Paramagnetic, Near-Infrared Fluorescent Mn-Doped PbS Colloidal Nanocrystals

Lyudmila Turyanska,* Fabrizio Moro, Andrew N. Knott, Michael W. Fay, Tracey D. Bradshaw, and Amalia Patanè*

The nanoscale design of nanocrystals by the controlled incorporation of dopant impurities is a research field of fundamental interest with great potential for numerous disruptive technologies.[1–3] In particular, 3d transition metal ions (Mn, Co, etc.) with their d-shell electronic configurations can imprint a nanocrystal with magnetic properties of relevance for innovative applications ranging from bio-imaging[4,5] to spintronics.[1,5] For example, colloidal nanocrystals doped with transition metals could provide versatile contrast agents for multimodal medical imaging, i.e., for contrast-enhanced magnetic resonance imaging (MRI) and confocal microscopy.[4] To date, a variety of nanoparticles (e.g., Fe_3O_4, FePt, $MnFe_2O_4$, and MnO) have been used for enhanced-contrast MRI,[5,6] but these require functionalization with fluorescent organic dyes for optical imaging and their solubility in physiological solvents demands modification of the nanocrystal surface. Luminescent, paramagnetic colloidal quantum dots, QDs (e.g., Mn-doped Si, ZnS, CdS/ZnS QDs) have also been previously studied.[7–9] However, these nanostructures require phase transfer to address water solubility and/or the visible photoluminescence (PL) emission limits their application in in vivo imaging due to strong photon absorption by biological tissues. Thus despite extensive research in this field, paramagnetic nanoparticles with fluorescence in the near-infrared (NIR) spectral region of the biological optical window are still not available.

In this work, we report paramagnetic, NIR fluorescent Mn-doped PbS colloidal nanocrystals in an aqueous solution. We demonstrate the successful incorporation of Mn atoms in the nanocrystals, which contain up to 8% Mn. The nanocrystals are optically active at room temperature in the technologically important biological window between 1.2 μm and 0.8 μm; also, the Mn atoms imprint the nanoparticles with paramagnetic properties. Preliminary cytoxicity studies show that the exposure of human cell lines to the nanoparticles at concentrations up to 0.2 mg mL^{-1} does not induce any adverse effect, thus providing guidelines on safe doses for further toxicology studies and future applications in medical imaging.

Our Mn-doped PbS nanocrystals in an aqueous solution differ from previously reported nanostructures based on PbS nanowires[10,11] and PbS nanocrystals in glass matrices[12,13] or in organic solvents.[14] To synthesize the Mn-doped PbS nanoparticles, we prepared a Pb^{2+} precursor solution containing 2.5×10^{-4} mol of lead acetate Pb(CH$_3$COO)$_2$, 1.5×10^{-3} mol of thioglycerol (TGL) and 5×10^{-4} mol of dithioglycerol (DTG) in 15 mL of deionized water, where the thiols act as capping agents.[15,16] The pH of the solution was adjusted to a value of 11.0 by addition of triethylamine. While maintaining the pH of the solution, manganese acetate Mn(CH$_3$COO)$_2$ salt was added with Mn concentration, x, up to 18%. To facilitate the incorporation of the Mn atoms during the nucleation stage of the nanocrystal growth, a 0.1 M solution of sodium sulfide Na$_2$S was added slowly to the reaction mixture at a molar ratio MR = 1:0.3 of Pb(Mn) to S. The synthesis was performed under N$_2$ flux with a concentration of nanoparticles of up to 10 mg mL^{-1}. The solutions were stored in a refrigerator at $T = 4$ °C under N$_2$ atmosphere and were found to be stable for at least 6 months. The solutions of the nanoparticles in bovine serum media used for the in vitro toxicity studies were also stable.

Figure 1a shows typical high-resolution transmission electron microscopy (HRTEM) images for Mn-doped PbS nanoparticles with average diameter d approximately equal to 5 nm. HRTEM, transmission electron microscopy (TEM), and selected area electron diffraction studies indicate that the nanocrystals retain the rock-salt crystal structure of bulk PbS and that the size distribution of the nanoparticles does not change following the incorporation of Mn. Size distribution profiles were obtained from analysis of the atomic force microscopy (AFM) images. The AFM study shows that the average nanoparticle diameter is $d = (4.5 \pm 1.8)$ nm for samples with $x = 0\%$, 5% and 10% (see Supporting Information). The incorporation of Mn in the nanocrystals was assessed by energy-dispersive X-ray (EDX) spectroscopy. The EDX spectra show the characteristic EDX peak associated with Mn at an energy of 5.9 keV (see Figure 1b). The Mn concentration, Mn$_{EDX}$, estimated from the analysis of the EDX data is smaller than x, i.e., only a fraction of Mn used in the precursor solution is incorporated in the nanocrystals.

Dr. L. Turyanska, A. N. Knott, Prof. A. Patanè
School of Physics and Astronomy
The University of Nottingham
Nottingham NG7 2RD, UK
E-mail: Lyudmila.Turyanska@nottingham.ac.uk;
Amalia.Patane@nottingham.ac.uk
Dr. F. Moro
School of Chemistry
The University of Manchester
Manchester M13 9PL, UK
Dr. M. W. Fay
Nottingham Nanotechnology and Nanoscience Centre
Nottingham NG7 2RD, UK
Dr. T. D. Bradshaw
School of Pharmacy
The University of Nottingham
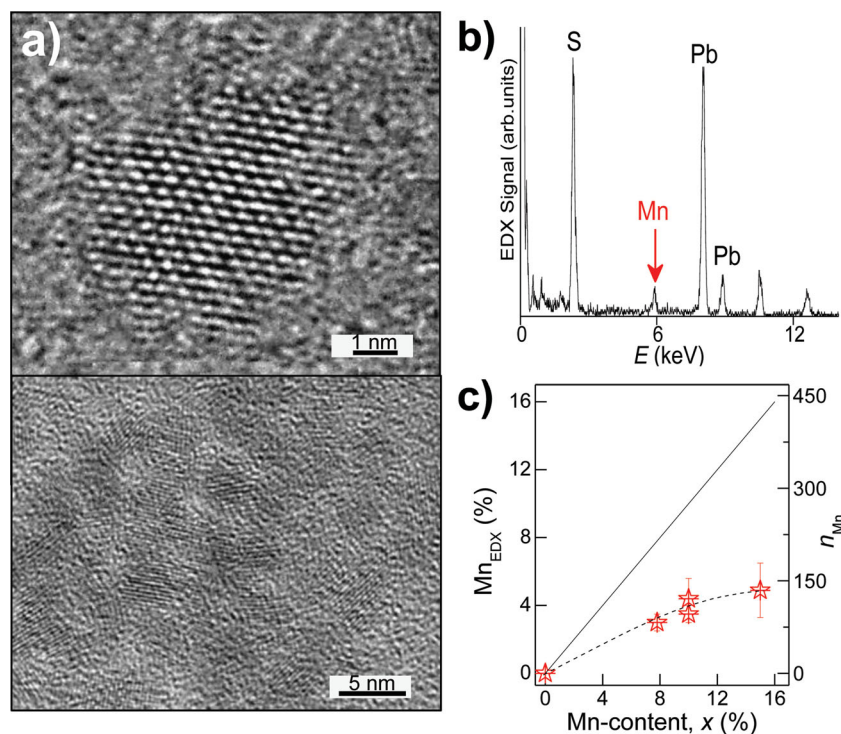Nottingham NG7 2RD, UK

Figure 1. a) HRTEM images and b) typical EDX spectrum of Mn-doped PbS nanoparticles. c) Comparison between the Mn content measured by EDX, Mn_{EDX}, (symbols) and the nominal Mn content (continuous line) at various x. The dashed line is a guide to the eye. The right axis represents the number of Mn ions per QD.

shows six narrow resonances superimposed on a broad background signal. These six lines are due to magnetic resonance transitions between states that are split by the hyperfine interaction between d-shell electrons ($S = 5/2$) and the nuclear spins ($I = 5/2$) of the Mn^{2+} ions. The asymmetric shape of the EPR lines indicates an additional unresolved hyperfine splitting due to the contribution from Mn ions on the surface and in the core of the nanoparticles. With increasing Mn content, the six resonances become broader until they merge into a single broad lineshape for $x = 5\%$ (see Figure 2a) and $x = 10\%$ (not shown) due to an increasing strength of Mn–Mn dipolar interactions. The simulation of the broad EPR spectra using a single Lorentzian lineshape indicates an hyperfine splitting constant $A = 9.25$ mT and a g-factor value of ≈ 2, similar to those reported before for Mn-doped PbS nanoparticles in glass matrix.[12] SQUID measurements confirm that the nanoparticles are paramagnetic: for $x = 10\%$, the magnetization tends to saturate for $B > 3T$ to a value of 6 emu g^{-1} at $T = 1.8$ K that decreases with increasing T (see Figure 2b). This value is much larger than that reported for nanoparticles in organic solution (0.5 emu g^{-1} for $x = 3\%$).[14]

Unlike Mn-doped II-VI nanocrystals,[1,2,7,17] the PL emission from the Mn dopants in PbS is either not observed or else is much weaker than the QD PL emission (**Figure 3**a,b): the weak Mn-related PL band is centered at ≈ 1.9 eV at room temperature, at higher energies relative to the much stronger PL emission

For example, $Mn_{EDX} = 4\%$ for $x = 10\%$, which corresponds to an average number of Mn ions per QD, $n_{Mn} = 110$ (Figure 1c). As can be seen in Figure 1c, the deviation of Mn_{EDX} from x increases for increasing Mn concentrations.

It is well established that there are fundamental limits to the doping concentrations that can be achieved in crystalline solids. Furthermore, the incorporation of dopant atoms into a single nanocrystal is governed by more complex mechanisms than in the bulk due to the large surface to volume ratio of the nanocrystals and a tendency of the dopants to migrate to the surface by a self-purification process.[17] Assessing the exact position of the dopants within a nanocrystal, i.e., core or surface, and their preferential site within the crystal lattice, is a challenging task that requires the development of sensitive microscopic techniques. This assessment is further complicated by the statistical distribution of the dopant concentration within an ensemble of nanoparticles. In this work, we focus on the magnetic and optical properties of ensembles of Mn-doped PbS nanoparticles, as probed by electron paramagnetic resonance (EPR) and PL for a wide range of Mn concentrations.

Figure 2a shows the room temperature K-band EPR spectra of Mn-doped PbS nanoparticles. For $x = 0.5\%$, the EPR spectrum
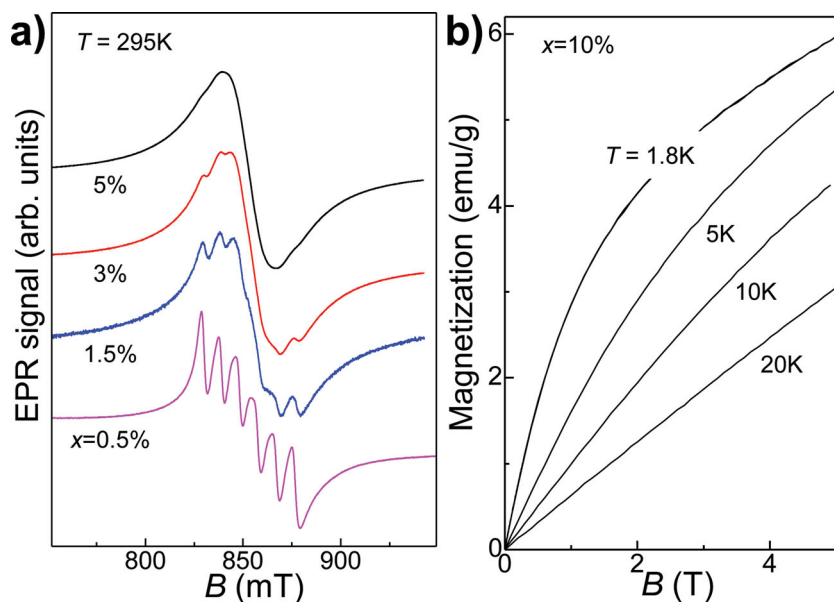

Figure 2. a) Room temperature ($T = 295$ K) K-band EPR spectra for Mn-doped PbS nanocrystals with x from 0.5 to 5%. Curves are displaced along the vertical axis for clarity. b) Magnetization as a function of magnetic field, B, at different temperatures, T, for $x = 10\%$.
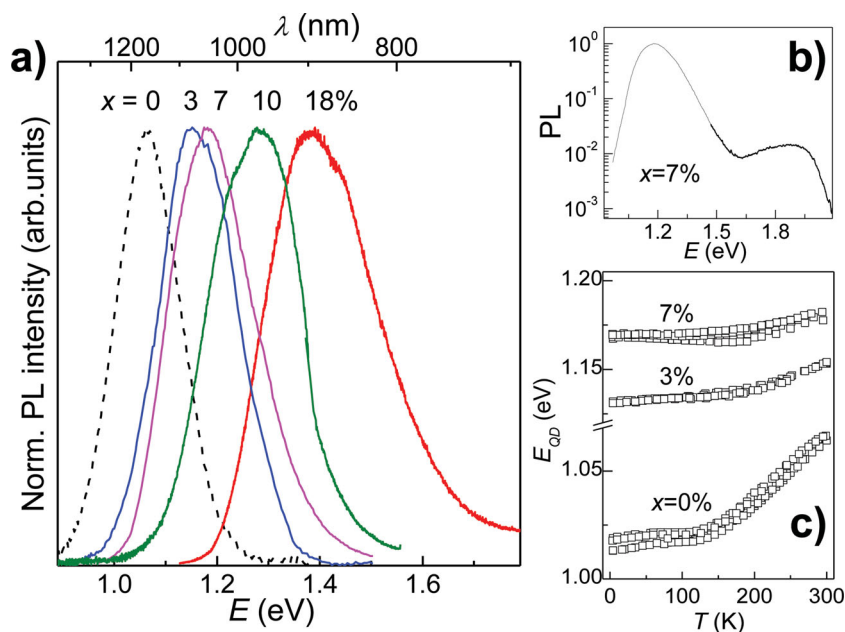
Figure 3. a) Normalized PL spectra of Mn-doped PbS nanocrystals with x from 0 to 18% (T = 295 K). b) PL spectrum for x = 7% showing the Mn-dopant PL emission at 1.9 eV and the QD PL emission at 1.2 eV (T = 295 K). c) Temperature dependence of the QD PL peak, E_{QD}, for x = 0, 3, and 7%.

For alloyed (PbMn)S nanoparticles, we expect a decrease of the temperature coefficient $\alpha = \partial E / \partial T$, describing the temperature dependence of the PL peak energy. In fact, the value of α is positive for bulk PbS (α^{PbS} = + 0.52 meV K^{-1}),[18] but negative for MnS (α^{MnS} = −2 meV K^{-1}).[19] As it can be seen in Figure 3c, for PbS QDs (no Mn), we observe an energy blue-shift of the PL band that is approximately linear for T > 100 K. This is described by the coefficient $\alpha_{\mathrm{QD}}^{\mathrm{PbS}} = \partial E_{\mathrm{QD}} / \partial T$ = + 0.3 meV K^{-1}, similar to that reported before for PbS QDs of similar size.[21–23] For samples incorporating Mn (x > 1%), the coefficient becomes significantly smaller, e.g., $\alpha_{\mathrm{QD}}^{\mathrm{PbMnS}}$ = + 0.12 meV K^{-1} for x = 7%. These observations do not depend on the laser excitation power used in the PL studies, which was varied over a wide range (i.e., P = 1–10^2 W cm^{-2}) in all experiments.

In summary, this study shows that the incorporation of Mn atoms in PbS nanocrystals has three main effects: i) it imparts the nanoparticles with paramagnetic properties; ii) it induces a blue-shift of the nanocrystal PL emission and a weaker temperature dependence of the PL peak energy due to the formation of alloyed nanoparticles; iii) also, it provides a means of tuning the PL emission of the nanocrystals in the technologically important biological window between 1.2 µm and 0.8 µm, never reported before for paramagnetic nanoparticles in an aqueous solution. Thus, these properties could offer possibilities for medical imaging applications. Since the future implementation of these nanoparticles for imaging of living organisms and cell lines is conditioned by the nanoparticle
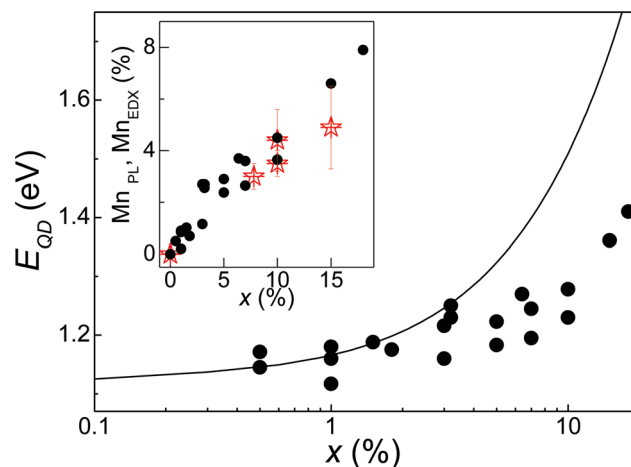
of the nanocrystals (see Figure 3b). Also, while the Mn-related PL band does not change with x, the QD PL emission tends to blue-shift with increasing x: for PbS QDs with no Mn, the PL band is centered at E_{QD} = 1.08 eV (λ = 1150 nm) at T = 295 K; increasing Mn results in a monotonic energy blue-shift of the PL emission up to a value of E_{QD} = 1.40 eV (λ = 885 nm) at x = 18% (see Figure 3a). Correspondingly, the PL intensity decreases by less than a factor of 10 going from x = 0 to 18%, thus indicating a low level of thermal escape of carriers from the dots and a low density of Mn-induced non-radiative recombination centers.

Since the TEM and AFM studies show that the average diameter and size distribution of the nanocrystals are not changed by the Mn incorporation, we attribute the blue-shift of the QD PL emission to a change in the composition of the nanocrystals. According to Vegard's law, the bandgap energy, E_g, of a (PbMn)S alloy with Mn fraction, x, is given by $E_g^{\mathrm{PbMnS}}(x) = (1 - x) E_g^{\mathrm{PbS}} + x E_g^{\mathrm{MnS}}$, where E_g^{PbS} = 0.41 eV and E_g^{MnS} = 3.10 eV are the bandgap energies at T = 295 K for bulk PbS and MnS, respectively.[18,19] The widening of the bandgap by Mn doping induces a corresponding increase of the exciton recombination energy, E_{QD}, which we estimate by using a simple spherical model,[20] i.e., $E_{\mathrm{QD}} = [E_g^2(x) + 2\hbar^2 E_g(x) \pi^2 m^{*-1} R^{-2}]^{1/2}$, m^* = 0.09 m_e where is an average effective mass and R = 2.5 nm is the QD radius. As shown in **Figure 4**, the calculated value of E_{QD} increases with increasing x and describes well the measured values of E_{QD} at small x (<3%). We attribute the disagreement at larger x to a partial incorporation of Mn in the nanocrystal: the Mn concentration, Mn$_{\mathrm{PL}}$, derived from the measured and calculated dependence of E_{QD} on x, is consistent with that derived from the EDX studies (Mn$_{\mathrm{EDX}}$), see inset of Figure 4. Thus, this analysis indicates an effective Mn content in the nanocrystals of up to 8%.

Figure 4. Dependence of the QD PL peak energy, E_{QD}, on x (T = 295 K). The continuous line represents the calculated dependence of E_{QD} on x according to the model described in the text. The inset shows the Mn content as estimated from EDX (Mn$_{\mathrm{EDX}}$, stars) and from the calculated and measured values of E_{QD} (Mn$_{\mathrm{PL}}$, dots). To account for different values of E_{QD} at x = 0%, in the calculation of E_{QD}, we have assumed QD radii in the range R = 2.5–2.6 nm.

Particle
& Particle Systems Characterization

www.particle-journal.com

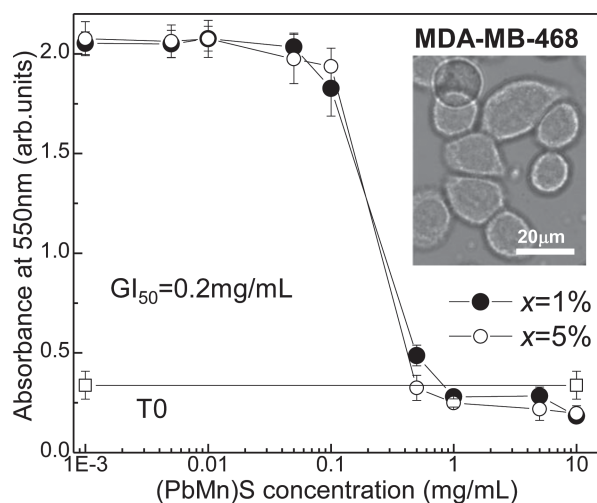*Materials Views*

www.MaterialsViews.com

COMMUNICATION

Figure 5. MTT assay for the human-derived breast cancer cell line MDA-468 exposed to Mn-doped PbS nanocrystals with $x = 1\%$ and 5% for 72 h. Error bars represent the standard deviation of the absorbance measured in eight wells. Inset: photograph of MDA-MB-468 cells.

toxicity,[24–26] we now present preliminary cytotoxicity studies in human cells.

We performed 3-(4,5-dimethylthiazol-2-yl)-2,5-diphenyltetrazolium bromide (MTT) assays on MRC-5 fetal lung fibroblast cells, which represent a normal phenotype, and on human-derived breast cancer MDA-MB-468 (ER-) and colorectal cancer HCT-116 cell lines. We assessed the cell viability after 72 h exposure of cells to (PbMn)S nanoparticles at concentration ranging from 0.001 mg mL^{-1} to 10 mg mL^{-1}, and different Mn content. **Figure 5** presents a typical cytotoxicity profile observed for MDA-MB-468 exposed to the Mn-doped PbS nanoparticles with $x = 1\%$ and 5%. For both cancerous cell-lines, we observe a sharp decrease in cell viability with 50% growth inhibition (GI_{50}) values of $\approx$0.2 mg mL^{-1}. The normal cell line (MRC-5) is more resilient with a GI_{50} value of 1 mg mL^{-1}. We note that the cell viability is not affected by the Mn content: the measured GI_{50} values are comparable to those for PbS QDs where apoptotic cell death is caused by the Pb^{2+}-induced increase in the reactive oxygen species (ROS).[24] Finally, the exposure of all cells to the nanoparticles at concentrations up to 0.2 mg mL^{-1} does not induce any adverse effect, thus providing guidelines on safe doses for further toxicology studies in living organisms.

In conclusion, we have shown that Mn atoms can be incorporated in colloidal PbS nanocrystals in an aqueous solution. These nanoparticles are paramagnetic and their EPR spectra reveal features characteristic of the hyperfine interaction of the *d*-electrons with the nuclear Mn spins. The blue-shift of QD PL emission with increasing Mn and the corresponding decrease of the PL energy shift with temperature indicate that alloyed (PbMn)S QDs are formed. The Mn atoms do not quench the NIR luminescence of the PbS QDs and imprint them with paramagnetic and optical properties tunable by the Mn content. This dual functionality and our preliminary results on cytoxicity in human-derived cell lines should stimulate further toxicology studies and future exploitation of these nanoparticles in medical imaging.

Experimental Section

Morphological Characterization: For the transmission electron microscopy (TEM) study, the nanoparticles were deposited on a lacey-carbon coated Cu grid or a graphene-coated grid, and TEM images were recorded on the JEOL1200EX and JEOL2100F microscopes operating at 120 kV. EDX spectra and maps were recorded with an Oxford Instrument ultrathin-window EDX detector. The energy-filtered TEM images were obtained using a Gatan Tridiem imaging filter. Prior to these experiments, solutions were extensively dialyzed against de-ionized water to remove excess salts. For the AFM studies, the nanoparticles were dip-coated onto Si substrates.

Optical and Magnetic Studies: Room temperature ($T = 295$ K) EPR measurements were recorded on a commercial Bruker E580 spectrometer. The measurements were carried out at K-band (23.9 GHz), with the microwave field B_1 perpendicular to the external magnetic field B (perpendicular mode), modulation amplitude of 0.5 mT and modulation frequency of 50 KHz. Magnetization measurements were carried out with a Quantum Design MPMS-XL5 superconducting quantum interference device (SQUID) magnetometer on pellet samples wrapped into Teflon tape, which has negligible diamagnetic contribution. These measurements were performed with magnetic fields B up to 5T. For PL experiments, the optical excitation was provided by the 514.5 nm line of an Ar$^+$ laser. The luminescence was dispersed by a 1/2 m monochromator and detected by a cooled (InGa)As photodiode or charge-coupled device (CCD) camera. As the QDs absorb over an extended wavelength range, their PL can be excited using different laser wavelengths up to the NIR wavelength range.

In Vitro Cytotoxicity Study: To probe the cytotoxicity of (PbMn)S, we performed MTT assays on MRC-5 fetal lung fibroblast cells, which represent a normal phenotype, and on human-derived breast cancer MDA-MB-468 (ER-) and colorectal cancer (HCT-116) cell lines. Cells were seeded into 96-well microtiter plates at a density of 5×10^3 per well and allowed 24 h to adhere. We assessed the cell viability after 72 h exposure to (PbMn)S with concentration in the range 0.001 mg mL^{-1} to 10 mg mL^{-1} and Mn content of 1%, 5%, and 8%. Serial dilutions of (PbMn)S were prepared in RPMI nutrient medium supplemented with 10% fetal bovine serum. Control wells received vehicle alone. Experimental plates were incubated at 37 °C for a further 72 h. Exposure times and seeding concentrations were chosen to maintain confluent monolayer of cells in the control well. Following exposure to the nanoparticles, MTT was added to each well at final concentration 400 µg mL^{-1} and plates incubated at 37 °C for 2 h to allow reduction of MTT by viable cell dehydrogenases to insoluble dark purple formazan crystals. Well supernatants were aspirated and cellular formazan solubilized by addition of DMSO (150 µL per well). Absorbance was read at $\lambda = 550$ nm using an Anthos Labtec systems plate reader. The measured intensity is proportional to metabolic activity, which correlates to cellular viability.

Supporting Information

Supporting Information is available from Wiley Online Library or from the author.

Acknowledgements

Materials
Views
www.MaterialsViews.com

Particle
& Particle Systems Characterization
www.particle-journal.com

COMMUNICATION

[1] D. A. Bussian, S. A. Crooker, M. Yin, M. Brynda, A. L. Efros, V. I. Klimov, *Nat. Mater.* **2009**, *8*, 35.

[2] J. H. Yu, X. Liu, K. Eun Kweon, J. Joo, J. Park, K.-T. Ko, D. Won Lee, S. Shen, K. Tivakornsasithorn, J. Sung Son, J.-H. Park, Y.-W. Kim, G. S. Hwang, M. Dobrowolska, J. K. Furdyna, T. Hyeon, *Nat. Mater.* **2010**, *9*, 47.

[3] W. K. Khalil, E. Girgis, A. N. Emam, M. B. Mohamed, K. V. Rao, *Chem. Res. Toxicol.* **2011**, *24*, 640.

[4] R. Koole, W. J. M. Mulder, M. M. van Schooneveld, G. J. Strijkers, A. Meijerink, K. Nicolay, *WIREs Nanomed. Nanobiotechnol.* **2009**, *1*, 475.

[5] J. Huang, X. Zhong, L. Wang, L. Yang, H. Mao, *Theranostics* **2012**, *2*, 86.

[6] C. Sun, J. S. H. Lee, M. Zhang, *Adv. Drug Delivery Rev.* **2008**, *60*, 1252.

[7] A. Louie, *Chem. Rev.* **2010**, *110*, 3146.

[8] M. Gaceur, M. Giraud, M. Hemadi, S. Nowak, N. Menguy, J. P. Quisefit, K. David, T. Jahanbin, S. Benderbous, M. Boissiere, S. Ammar, *J. Nanopart. Res.* **2012**, *14*, 932.

[9] N. Erathodiyil, J. Y. Ying, *Acc. Chem. Res.* **2011**, *44*, 925.

[10] S. K. Mandal, A. R. Mandal, S. Banerjee, *ACS Appl. Mater. Interfaces* **2012**, *4*, 205.

[11] D. Isheim, J. Kaszpurenko, D. Yu, Z. Mao, D. N. Seidman, I. Arslan, *J. Phys. Chem. C* **2012**, *116*, 6595.

[12] R. S. Silva, P. C. Morais, F. Qu, A. M. Alcalde, N. O. Dantas, H. S. L. Sullasi, *Appl. Phys. Lett.* **2007**, *90*, 253114.

[13] N. O. Dantas, F. Pelegrini, M. A. Novak, P. C. Morais, G. E. Marques, R. S. Silva, *J. Appl. Phys.* **2012**, *111*, 064311.

[14] G. Long, B. Barman, S. Delikanli, Y. Tsung Tsai, P. Zhang, A. Petrou, H. Zenga, *Appl. Phys. Lett.* **2012**, *101*, 062410.

[15] L. Turyanska, T. D. Bradshaw, J. Sharpe, M. Li, S. Mann, N. R. Thomas, A. Patanè, *Small* **2009**, *15*, 1738.

[16] L. Bakueva, I. Gorelikov, S. Musikhin, X. S. Zhao, E. H. Sargent, E. Kumacheva, *Adv. Mater.* **2004**, *16*, 926.

[17] N. Pradhan, D. D. Sarma, *J. Phys. Chem. Lett.* **2011**, *2*, 2818.

[18] O. Madelung, in *Semiconductors: Data Handbook*, 3rd edn., Springer, London **2003**, Ch. 23, p. 586.

[19] S. Mochizuki, N. Takayama, *J. Phys.: Condens. Matter.* **1991**, *3*, 2729.

[20] Y. Wang, A. Suna, W. Mahler, R. Kasowski, *J. Chem. Phys.* **1987**, *87*, 7315.

[21] B. Ullrich, J. S. Wang, G. J. Brown, *Appl. Phys. Lett.* **2011**, *99*, 081901.

[22] M. N. Nordin, J. R. Li, S. K. Clowes, R. J. Curry, *Nanotechnology* **2012**, *23*, 275701.

[23] A. Olkhovets, R.-C. Hsu, A. Lipovskii, F. W. Wise, *Phys. Rev. Lett.* **1998**, *81*, 3539.

[24] L. Turyanska, T. D. Bradshaw, M. Li, P. Bardelang, W. C. Drewe, M. W. Fay, S. Mann, A. Patanè, N. R. Thomas, *J. Mater. Chem.* **2012**, *22*, 660.

[25] R. Hardman, *Environ. Health Perspect.* **2006**, *114*, 165.

[26] K.-T. Yong, W.-C. Law, R. Hu, L. Ye, L. Liu, M. T. Swihart, P. N. Prasad, *Chem. Soc. Rev.* **2013**, *42*, 1236.